Dissolution of olivines from steel and

copper slags in basic solution

2

Brian Traynor a*, Ciara Mulcahy a, Hugo Uvegi a, Tunahan Aytas a, Nicolas Chanut b, Elsa Olivetti a 3 4 5 ^a Department of Materials Science and Engineering, Massachusetts Institute of Technology, 77 6 Massachusetts Avenue, Cambridge, Massachusetts, 01239, United States 7 8 ^b Department of Civil and Environmental Engineering/MIT Energy Initiative, Massachusetts Institute 9 of Technology, 77 Massachusetts Avenue, Cambridge, Massachusetts, 01239, United States 10 11 * Corresponding author. Email: elsao@mit.edu 12 Keywords: pH; kinetics; surface layer; Ca₂SiO₄ 13 14 This study explores the effect of aqueous chemical environment on the dissolution rate of the minerals 15 γ -C₂S and fayalite, identified as primary phases of ladle furnace steel slag and copper slag. γ -C₂S and 16 favalite were exposed to solutions of NaOH and Ca(OH)2, chosen to mimic the pore solutions of 17 18 alkali-activated and Portland-cement based binders. While both from the olivine mineral group, γ-C₂S 19 and fayalite displayed opposing dissolution trends with respect to pH. The rates of γ-C₂S dissolution 20 were observed to decrease with higher pH, while fayalite dissolution rates increased with pH, and both relationships were described via empirical functions of the form $R = k \cdot a_{H^+}^n$. The contrasting 21 22 dependence of dissolution rate on pH for both minerals was attributed to the formation of chemically distinct surface layers on both minerals during dissolution. These results have significance for 23

blending of slags with high olivine contents in binders with a range of aqueous chemical environments.

1. Introduction

Cement production has been identified as a sector in which widescale reductions in greenhouse gas emissions will be difficult to achieve due to existing economies of scale [1]. An analysis by the United Nations Environment Program Sustainable Building and Climate Initiative concluded that increased use of supplementary cementitious materials (SCMs) as replacement for Portland cement clinker and more efficient use of Portland cement clinker in concretes represent the best strategies for reduction of CO₂ emissions [2]. Providing a sufficient supply of SCMs to the cement industry is a challenge as the traditionally used SCMs, fly ash and blast furnace slag, are either well-used [3] or have threatened supply chains [4]. The range of potential SCMs has been broadened by the research community to meet this growing demand, encompassing calcined clays, biomass ashes, steel slags, non-ferrous slags, and bauxite residues. Two industrial wastes produced in large volume but with minimal use as SCMs are steel slag and copper slag [5]. Steel and copper slags are produced in massive and increasing quantities; steel slag production is estimated to be equal to 10-15% of total steel production, putting global steel slag production at 190-290 million metric tons in 2018 [6], while global copper slag production is 35-40 million metric tons in 2018 [7] (based on 2.2-2.5 tons of copper slag for every ton of copper [8,9]).

The scale of global steel and copper slag production has prompted research efforts aimed at identifying suitable concretes in which to use these materials. As an umbrella term, steel slag encompasses an array of slags, including but not limited to basic oxygen furnace slag, electric arc furnace slag, and ladle furnace slag (LFS). In this study, we focus on LFS because of its mineralogy and previously demonstrated application in concretes. The physical and chemical properties of LFS,

as well as its applications in construction materials, have been reviewed, and interested readers are referred to [10]. LFS has been identified as weakly cementitious when used in Portland cement based concretes or blended with blast furnace slag [11,12]. Alkali activation of LFS has also been investigated, where increases in activator concentration resulted in mortars with higher compressive strength [13,14]. Similarly, the properties and utilization of copper slag have been reviewed before and interested readers are referred to [8,15,16]. In general, copper slag is characterized as an inert material with good performance as an aggregate with little to no cementitious properties [15]. Much research into copper slag usage has centered around its use as a fine aggregate replacement, with studies generally observing improved technical performance at low replacement [17–19]. Efforts have been made to chemically activate copper slags in the same manner as has been successfully implemented for fly ash and blast furnace slag, although with limited success [20,21]. Studies using amorphous copper slags have reported the synthesis of load-bearing inorganic polymers formed with the aid of an activating solution [22,23]. Despite the work done to date on the performance of these slags in various concretes, there remains an important gap in the understanding of their reactivity in the aqueous chemical environments typical of Portland-cement or alkali-activated pore solutions. As dissolution of a precursor is the first step in the development of strong, load-bearing binder, understanding how these materials dissolve and how dissolution rates are affected by the aqueous environment is key to their effective use [24,25].

68

69

70

71

72

73

74

75

76

50

51

52

53

54

55

56

57

58

59

60

61

62

63

64

65

66

67

While steel slag and copper slag are heterogeneous materials, the mineral phases of both come from only a few mineral groups. Here, we focus on the primary mineral phases of LFS and copper slag; γ -C₂S (calcio-olivine, γ -Ca₂SiO₄) and fayalite (Fe₂SiO₄), respectively. The reasons for studying the dissolution kinetics of these two minerals are twofold. First, γ -C₂S and fayalite are the primary phases of their respective slags, meaning that the dissolution kinetics of these mineral phases will have a major impact on the dissolution of the overall slag [11]. Second, γ -C₂S and fayalite are both members of the same mineral group; the olivines. While these two minerals have been the subject of limited research, a third mineral in the olivine mineral group, forsterite (Mg₂SiO₄), has been widely studied

by geochemists due to its prominence in the earth's crust. As members of the same mineral group, γ
C₂S, fayalite, and forsterite are all expected to exhibit similar properties and reactivity in solution [26–

28]. Past work on forsterite is therefore pertinent to this work on γ-C₂S and fayalite. Most studies of

forsterite dissolution are in acidic solutions and previous studies [29] have shown the mechanism of

olivine dissolution at low pH to proceed through ion exchange of metal cations with H⁺ ions in

solution. In this region, the rate of dissolution has been described as a function of H⁺ ion activity,

described in Eq (1);

$$84 R = k \cdot a_{H^+}^n (1)$$

where R is the rate of dissolution of olivine, k is the rate coefficient, a_{H^+} is the activity of H^+ in solution, and n is an empirically determined constant. Eq (1) is typically plotted in the form of $log(R) = log(k) - n \cdot pH$, meaning that a positive value of n implies that dissolution rates decrease with higher pH. For forsterite dissolution in acidic solutions, n has been reported in the range 0.46 to 0.54 [30]. Eq (1) has also been used to describe the dependence of dissolution rate as a function of pH in basic solutions. The value of n for forsterite dissolution in basic solutions has been the subject of fewer studies, but has been variously proposed to be 0.22 [31], 0.25 [30] and -0.39 [32], demonstrating a lack of consensus. Decreasing rates of dissolution at higher pH is a behavior contrary to the majority of silicates [33]. Despite extensive studies of forsterite at low pH, γ -C₂S and fayalite, while common in slags, are comparatively understudied. Westrich et al. calculated a value for n of 0.42 for γ -C₂S in acidic solutions, but to the best of our knowledge no studies have reported rates of γ -C₂S as a function of pH in basic solutions. Several studies have investigated the hydraulicity of γ-C₂S by means of calorimetry [34–36]. Fayalite has been studied both in acidic and basic solutions, often with conflicting conclusions. In acidic solution, positive values of n have been reported (0.69 and 0.74) [37,38]. An increase in dissolution rate at higher pH (n of -0.39 [39] and -0.31 [37]) has been proposed based on comparison with other iron silicates, but not experimentally confirmed.

85

86

87

88

89

90

91

92

93

94

95

96

97

98

99

In this study, we explore the effect of the aqueous environment on the rate of dissolution of γ -C₂S and fayalite. The dependence of dissolution rate on pH are measured in NaOH and Ca(OH)₂ solutions designed to mimic the aqueous environments typical of Portland-cement (moderate pH, high Ca) and alkali-activated (high pH, low Ca) binders. By understanding how these minerals react in basic solutions, the reactivity of slags with high olivine content can be anticipated for a range of aqueous chemical environments typical of traditional and alternative binders.

2. Materials and Methods

2.1 Materials

LFS consists of multiple calcium silicate minerals (including diopside, merwinite, wollastonite and larnite), with γ -C₂S often present as the major phase. In order to focus on this dominant phase, a synthetic γ -C₂S was used to study γ -C₂S dissolution kinetics in this work. In contrast, fayalite is typically the only silicate phase present in copper slag. In this study, both a synthetic fayalite and a fayalitic copper slag (referred to as fayalite slag) were used to study the dissolution kinetics of fayalite.

All γ -C₂S powders were synthesized using the modified Pechini synthesis method, based on the method described by Nettleship et al. [40,41]. Stoichiometric quantities of Ca(NO₃).4H₂O (19.543 g) (>99.995%, Alfa Aesar) and colloidal silica (7.421 g of 34 wt% colloidal silica) (LUDOX TMA, Sigma Aldrich) were combined in a beaker with 150 mL of deionized water. The solution was stirred at 240 rpm, and brought to a boil in a water bath. Citric acid (91.3 g) (ACS reagent, \geq 99.0%, Sigma Aldrich) was added to the solution, which was then covered using aluminum foil. The solution was stirred for 30 minutes, after which the foil was removed and ethylene glycol (60.876 g) (Fisher

Scientific) was added. Throughout the process, the water bath was repeatedly replenished until the solution started to turn viscous (several hours), at which point the solution (now gel) was poured into silicone molds. The gel was dried out completely in a drying oven at 170 °C for 24 hours before being ground up in a mortar and pestle and calcined at 1400 °C for 6 hours. The powder was calcined 4 times to achieve a pure γ -C₂S phase. The product was washed repeatedly in isopropanol to remove smaller particles (<1 µm) from the surface of the γ -C₂S powder.

The chemical composition of the fayalite slag (source: Hindalco Industries, Mumbai, India) as determined by XRF is shown in Table 1. Chemical composition was determined on an Axios PANalytical XRF (based on dry material in its most stable oxidation state). Fe is reported as Fe₂O₃ although it is present as Fe(II) in fayalite. The fayalite slag was ground for 5 minutes in a SPEX tungsten carbide grinding vial set and washed repeatedly with isopropanol to remove smaller particles (<1 μm) prior to dissolution tests. The synthetic fayalite was synthesized using Fe (<212 μm, Acros Organics, 99%), Fe₂O₃ (30-50 nm, Alfa Aesar, 98%) and SiO₂ (<0.5 μm, Alfa Aesar, 99.9%) precursors. Precursor powders were subjected to 30 minutes of high energy ball milling under argon atmosphere in a SPEX tungsten carbide grinding vial set. The powder was heated to 750 °C under argon atmosphere for 24 hours. The heating cycle was repeated 3 times and the powder ball milled under argon atmosphere between each heating cycle.

Table 1. XRF composition of fayalitic copper slag.

Oxide	wt%	mol% (excl. LOI)
Na ₂ O	0.34	0.61
MgO	1.13	3.12
Al_2O_3	2.83	3.09
SiO_2	21.68	40.20

SO_3	1.91	2.66
K ₂ O	0.78	0.92
CaO	1.76	3.50
TiO ₂	0.24	0.33
Fe ₂ O ₃	59.94	41.82
CuO	0.83	1.16
MoO_3	0.31	0.24
PbO	0.24	0.12
ZnO	0.86	1.18
LOI	6.25	0

Phase composition was determined by X-ray powder diffraction (XRPD). XRPD data was collected using high speed Bragg-Brentano optics on a PANalytical X'Pert Pro MPD operated at 45 kV and 40 mA. HighScore Plus software was used for quantitative X-ray diffraction (QXRD) using Rietveld analysis [42]. γ -C₂S was synthesized to a purity of > 98%, with the remainder β -C₂S impurities. The synthesized fayalite was found to be > 99% fayalite, with metallic iron being the only impurity detected. The major mineral phase of the fayalite slag was fayalite. Minor phases of sodium sulfate, hematite and copper metal were detected through a combination of XRPD and SEM-EDS analysis. X-ray diffractograms for all three materials are included in the Supplementary Information.

The presence of an amorphous iron-silicate phase in the fayalite slag could not be definitively identified. However, such a glassy phase would be likely to have an impact on the overall dissolution rate of the slag. As the material of interest in this study is fayalite, dissolution rates of both pure synthetic fayalite and fayalite slag were compared.

Krypton adsorption measurements at 77K were carried out using a Micromeritics 3Flex surface characterization analyzer (Micromeritics Instruments Corporation) to assess the specific surface area

of the samples. Prior to the measurements, the samples were activated under secondary vacuum at 200° C for 12 hours. The Kr adsorption isotherms collected were interpreted using multi-point Brunauer-Emmett-Teller (BET) analysis for surface area determination [43] over the range 0.06–0.20 relative pressure (P/P₀) and with a Kr cross-sectional area of 0.210 nm². The determination of the minimum amount of sample needed was based on previous calibration of the instrument published in the Supplemental information of [44]. This calibration was achieved by varying the amount of an alumina reference material provided by the manufacturer that exhibits a calibrated surface area of 0.22 ± 0.03 m² g⁻¹. A minimum absolute sample area of 0.04–0.05 m² in the sample cell was needed in order to obtain reliable results. In our case, the surface area of the samples varied from 0.4 m² g⁻¹ to 0.04 m² g⁻¹ corresponding to a mass of sample needed from 15 mg to 100 mg depending on the considered material. To ensure the reliability of the results obtained, 0.0400 mg have been used for each sample. Particle size distributions are included in the supplementary information and were recorded using a laser-diffraction particle size analyzer (Beckman Coulter Inc., LS 13320).

2.2 Dissolution

The dissolution behavior of the powders was investigated in different aqueous environments: γ -C₂S in 0.0001 M (mol Na/L), 0.0005 M, 0.001 M, 0.005 M, 0.01 M, 0.05 M, 0.1 M, 0.5 M NaOH solutions and 0.001 M (mol Ca/L), 0.0017 M, 0.0038 M, and 0.012 M Ca(OH)₂ solutions; and both fayalite materials in 0.0001 M (mol Na/L), 0.001 M, 0.01 M, and 0.1 M NaOH solutions. All solutions were bubbled with N₂ gas for a minimum of 30 minutes prior to dissolution experiments and all experiments were performed under N₂ atmosphere in a glove box to reduce any potential carbonation. The dissolution experiments were performed at liquid:solid ratios of 10,000:1 in batch reactors to prevent precipitation of reaction products, e.g. calcium silicate hydrate (CSH). 0.05 g of powder was added to 500 mL of solution to initiate dissolution. 5 mL of solution was removed at specified

190 intervals for further analysis and the solution was immediately replenished with 5 mL of pure 191 solution. Samples were not stirred to avoid particle abrasion. 192 193 An Agilent 5100 Vertical Dual View ICP-OES with an autosampler was used to analyze elemental 194 concentrations of relevant elements during dissolution. Calibration standards were prepared from two 195 standard solutions: one containing 1000 mg/L Si in H₂O and one containing 1000 mg/L each of Ca, 196 Al, Na, K, Mg, Fe, and S in 4% HNO3 (Elemental Scientific, Omaha, NE). 197 198 Solution pH's were measured using a Thermo Orion Ag/AgCl combination triode with Automatic 199 Thermal Correction probe stored in KCl solution. Alkali error from measurements of the 0.1 and 0.5 200 M NaOH solutions was accounted for by calibration of the pH meter using NaOH solutions of known 201 concentration. 202 203 The morphologies and particle sizes of the powders were imaged using scanning electron microscopy 204 (SEM). Powders were packed onto carbon tape and imaged on a JEOL 6610 Low Vacuum SEM 205 equipped with an EDAX detector and energy-dispersive X-ray spectrometer (EDS). 206 207 Surface chemistries were measured using a Thermo Scientific K-Alpha+ XPS with an Al K-alpha X-208 ray source and a beam spot size of 400 µm. Samples were filtered, washed in ethanol and dried under 209 vacuum for several hours at ambient temperature. Powders were packed onto Cu tape for analysis. 210 Elemental concentrations were calculated using the Avantage program. 211 212 GEM-Selektor v3.3 (http://gems.web.psi.ch/) [45,46] with PSI-Nagra [47] and Cemdata18 [48] databases were used to calculate ion activity products. The aqueous electrolyte model used to 213 214 determine the activity of ions in solution was the extended Helgeson form of the Debye-Hückel

215 equation with ion size and extended term parameters of NaOH background electrolyte (å = 3.31 Å and 216 $b_{\gamma} = 0.098 \text{ kg mol}^{-1}$) [49]. The osmotic coefficient and the Debye-Hückel extended term were used to calculate the activity of water and neutral species respectively. 217 218 219 3. Results 220 221 3.1 γ-C₂S dissolution 222 223 The effect of pH on the dissolution rate of γ -C₂S in NaOH and Ca(OH)₂ is shown in Figure 1. Dissolved Si (Figure 1A) and Ca (Figure 1B) concentrations are reported in NaOH solution. The high 224 225 background concentration of Ca in Ca(OH)₂ solutions resulted in an insignificant change in overall Ca concentrations from dissolved Ca, and only Si concentrations are reported for Ca(OH)₂ solutions. 226 227

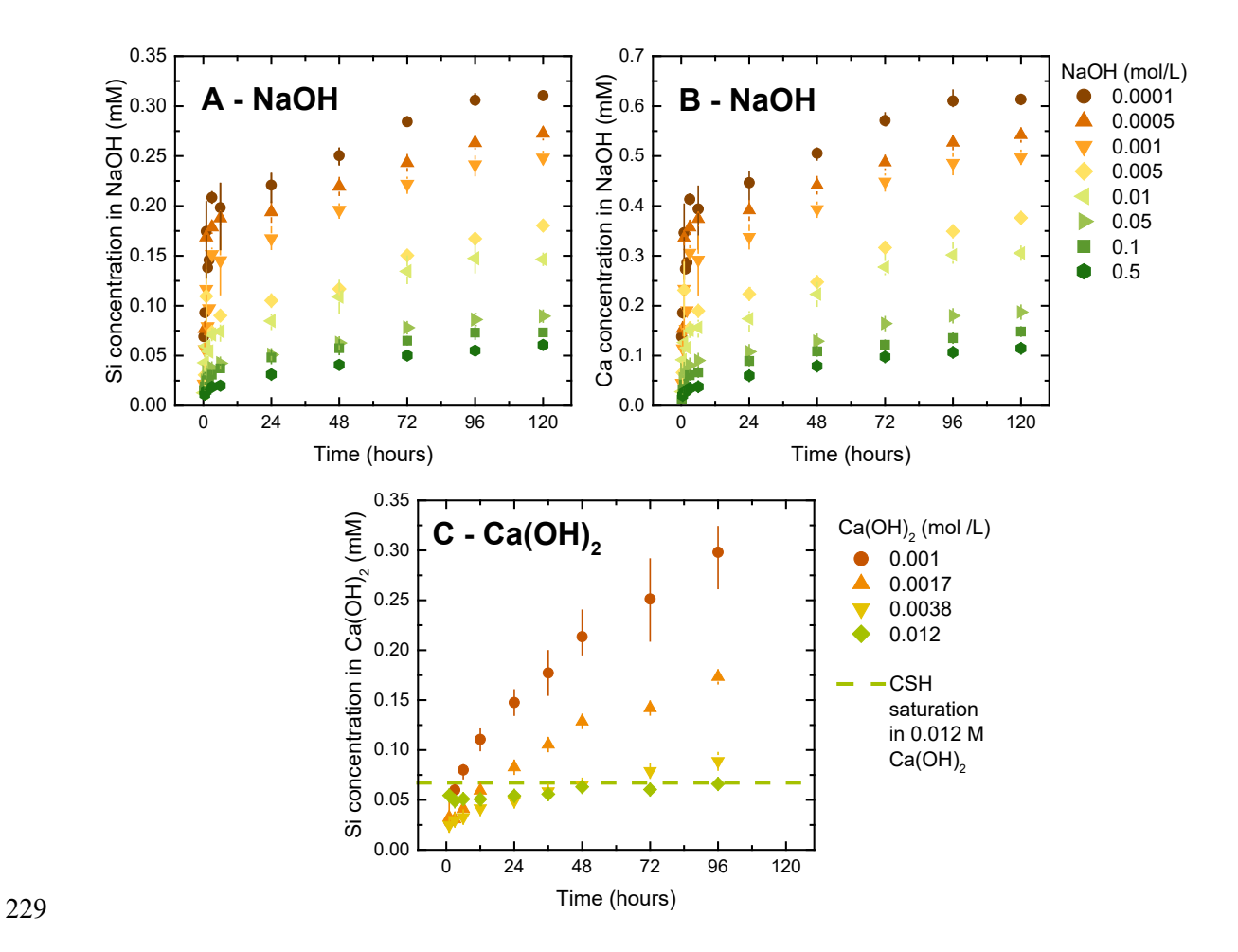


Figure 1. Dissolution kinetics of γ -C₂S in solutions of NaOH (A and B) and Ca(OH)₂ (C) at liquid:solid ratios of 10,000:1. Dissolved Si and Ca concentrations (milli-molarity) are shown as a function of time for different solution molarities. Saturation states for calcium silicate hydrate (CSH) are represented by the horizontal dotted lines. As CSH was only predicted to precipitate in the 0.012 M Ca(OH)₂ experiment, it is the only solution for which the CSH saturation is shown. Error bars

represent maximum and minimum values of triplicate experiments.

For both NaOH and Ca(OH)₂ solutions, the dissolution of γ-C₂S is slower when the pH increases. For all NaOH molarities, a fast dissolution rate is observed during the first 6 hours. Dissolution slows to a constant rate between 6 hours and 96 hours and rates appear to decrease beyond 96 hours. In Ca(OH)₂ solutions, Si concentrations did not increase rapidly up to 6 hours as in NaOH solutions. The rate of Si

dissolution in Ca(OH)₂ reaches a steady-state between 6 and 48 hours, before decreasing slightly. We refer here to the constant rate of dissolution as the "steady-state" regime. Dissolution in NaOH solutions proceeds congruently within the uncertainty of the ICP-OES measurements. Changes in Ca concentration due to γ-C₂S dissolution were obscured by the high background concentration of Ca in the Ca(OH)₂ solutions. It is not known with certainty if dissolution in Ca(OH)₂ solutions proceeded congruently. The rapid dissolution during the first 6 hours in NaOH solutions is likely due to one of: i) dissolution of small particles with high specific surface area that completely dissolve within the first few hours; ii) dissolution of impurity β -C₂S which dissolves orders of magnitude more rapidly than γ -C₂S. The apparent decrease in rate beyond 96 hours of dissolution in NaOH solutions appears to be due to depletion of starting material – 0.3 mM of Si in solution corresponds to 50% of the starting material. The decrease in rate in Ca(OH)₂ happens earlier and may also be due to depletion of the starting material, but it is not clear if this is the case. It is worth noting that no phases are expected to precipitate in either NaOH or Ca(OH)₂ solutions at these concentrations based on calculated saturation states of relevant phases (as calculated in GEMSelektor). Growth of a surface layer, either through formation of a leached layer or a precipitated secondary mineral, that slows dissolution at later ages is the most likely explanation for this trend. This is discussed below. Only in 0.012 M Ca(OH)₂ after 48 hours are reaction products in the form of calcium silicate hydrate (based on the solid solution model of [50]) expected to precipitate. Otherwise, no reaction products are expected in the other NaOH or Ca(OH)₂ solutions. The pH of the 0.0001 M, 0.0005 M and 0.001 M NaOH solutions rose from values of 10, 10.85, and 11.11 to 10.93, 11.07, and 11.21, respectively, by 6 hours of dissolution due to formation of OH⁻ ions in solution following Ca²⁺ dissolution from the γ-C₂S. There was no discernible change in the pH over time for the other NaOH and Ca(OH)₂ solutions.

263

264

265

266

267

241

242

243

244

245

246

247

248

249

250

251

252

253

254

255

256

257

258

259

260

261

262

Scanning electron micrographs of γ -C₂S particle surfaces after 120 hours of exposure to NaOH and Ca(OH)₂ solutions are shown in Figure 2. Powders exposed to lower pH solutions are more etched, indicating greater extent of dissolution in agreement with the ICP-OES data discussed above. The formation of etch pits on a dissolving surface is well documented in the literature as a mechanism for

mineral dissolution at far from equilibrium conditions [51–55]. The smaller extent of pitting on the particles at higher pH suggests weaker driving force for dissolution, and lower extent of dissolution than in low pH solutions. There is also no evidence of formation of reaction products at this length scale.

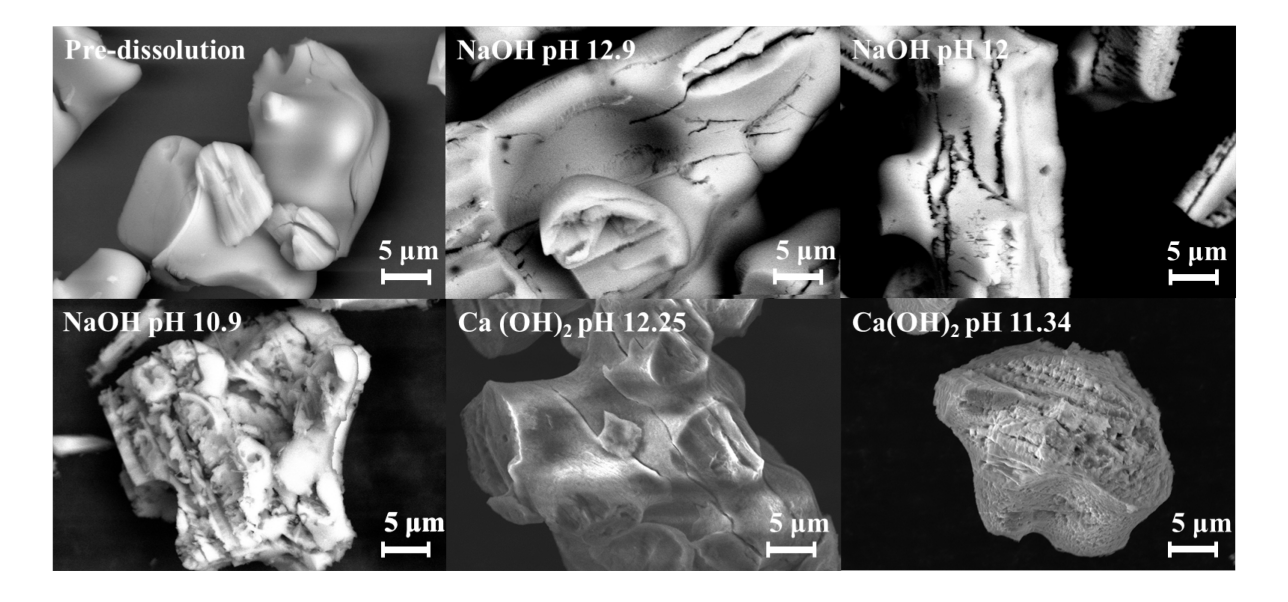


Figure 2. Scanning electron micrographs of γ - C_2S pre- and post-exposure to NaOH or Ca(OH)₂ solutions of varying pH.

Changes in the surface chemistry of the calcium silicate particles as a function of time were monitored using X-ray photoelectron spectroscopy. Table 2 shows the Ca/Si ratio at the surface of calcium silicate powders exposed to pH 10 and pH 11 NaOH. The Ca/Si ratio for the pristine powder has been normalized to 2 (the Ca/Si ratio of the dissolving mineral) and all other Ca/Si ratios scaled accordingly. The Ca/Si ratio decreases over time and the change is more pronounced in lower pH solutions with greater extents of dissolution. The electron escape depth for SiO₂ is on the order of 2.6 nm [56], and Zakaznova-Herzog et al. estimated the analysis depth for olivines and pyroxenes to be on the order of 7.8 nm (x3 the electron escape depth) for an Al K-alpha source [57]. This analysis

depth represents tens of monolayers at the surface a depth which is likely to partly obscure surface specific chemistry. Further interpretation of these results will be discussed below.

Table 2. Ca/Si ratios at the surface of the sample as measured by XPS. Errors are based on the range observed from 10 measurements.

	ratio (pH 10	Ca/Si atomic ratio (pH 11 NaOH)
Pre-dissolution	2.00±0.07	2.00±0.07
1 day exposure	1.85±0.03	1.96±0.02
7 days exposure	1.54±0.04	1.74±0.04

3.2 Fayalite Dissolution

The effect of pH on the dissolution rate of fayalite slag and synthetic fayalite is shown in Figure 3A and 3B respectively. Fe data is not reported as goethite (α -FeO(OH)) is known to precipitate at very low Fe concentrations in basic solutions, and no meaningful kinetic information can be discerned from Fe concentrations.

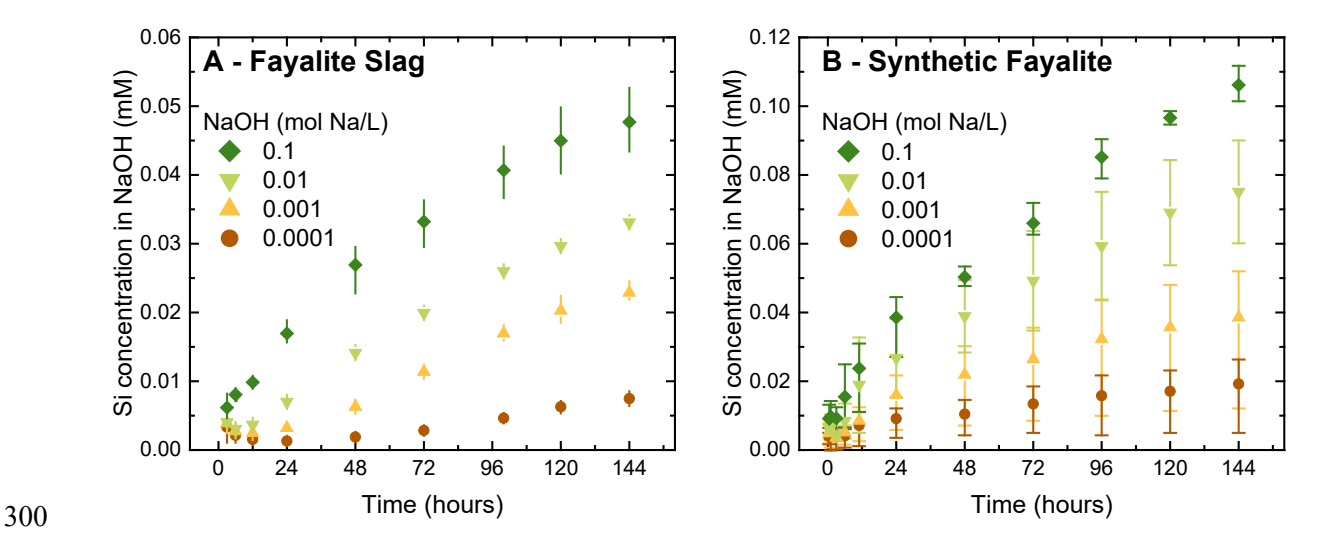


Figure 3. Dissolution kinetics of; A – fayalite slag and B – synthetic fayalite, in solutions of NaOH at liquid:solid ratios of 10,000:1. Dissolved Si concentrations (milli-molarity) are shown as a function of time for different solution molarities. Error bars represent maximum and minimum values of triplicate experiments.

While the rate of fayalite dissolution is pH dependent, the trend is opposite to that of γ -C₂S with fayalite experiencing faster dissolution at higher pH. Approximately steady-state dissolution occurs between 12 and 72 hours at each NaOH molarity. The reason for initial decreases in Si concentration during fayalite slag dissolution from 3 to 6 hours for 0.0001 M, 0.001 M, and 0.01M solutions is not known. At later age, the most likely reason for the decline in dissolution rate is the growth of a goethite precipitate layer on the surface of the fayalite particles which inhibits dissolution. The surfaces of both the synthetic fayalite and fayalite slag particles were imaged using SEM pre- and post-dissolution, although no discernible difference was observed. Possible reasons for the different dissolution behavior of γ -C₂S and fayalite are discussed below.

4. Discussion

4.1 Rate of dissolution in basic media

The rate of dissolution of γ -C₂S was calculated from the steady-state dissolution regime using Eq (2);

321
$$R \text{ (moles } cm^{-2}s^{-1}) = \frac{\Delta C_i}{\Delta t} \frac{V_{soln}}{A_{BET} m \nu_i}$$
 (2)

where ΔC_X (mol L^{-1}) is the change in element i concentration over change in time Δt (s), V_{soln} (L) is the volume of the solution, A_{BET} (cm^2 g^{-1}) is the specific surface area of the powder from BET, m (g) is the mass of powder in solution, and v_i is stoichiometry of element i in the dissolving olivine ($v_{Ca} = 2$, $v_{Si} = 1$). BET specific surface areas of γ -C₂S and fayalite slag were measured to be 0.42±0.01 (cm^2 g^{-1}) and 0.59±0.01 (cm^2 g^{-1}), respectively.

Rates of dissolution of γ -C₂S as a function of pH in NaOH, Ca(OH)₂ and acid solutions are shown in Figure 4A. Rates of dissolution of in NaOH and Ca(OH)₂ solutions are from this study while rates in acid are from Westrich et al [58], the only other study that reported γ -C₂S dissolution rates, to the authors' knowledge. Linear fits are based on the form of Eq (1), with the slope corresponding to n. Calculated rates use Si concentrations in solution. The average value of n for NaOH solutions across all experiments was 0.24, although values from 0.18 to 0.33 were calculated from repeat experiments. This result agrees with reported forsterite dissolution rates as a function of pH in basic solution, where values of n = 0.25 are typically reported [30]. For Ca(OH)₂ solutions, the average value of n was 1.2, with values from 1.17 to 1.25 being measured. γ -C₂S rates are fitted with a slope of 0.5 in acidic pH [58] in line with the vast majority of experimentally determined values of n = 0.5 for forsterite dissolution [30]. The rates of the dissolution in acid and NaOH solutions approximately converge at neutral pH. In contrast to γ -C₂S dissolution rates, fayalite dissolution was faster at higher pH. Rates of fayalite dissolution are complicated by the redox chemistry of iron, as has been reported previously in the literature [37,39,59,60]. Rates of fayalite slag and synthetic fayalite dissolution as a function of pH are shown in Figure 4B. The model of Wogelius and Walther [37] shown in Figure 4B is not based on

experimentally measured rates and is an extension of a model for fayalite dissolution in acidic solution. This extension assumed that the rate as a function of pH in basic solution follows a rate law of the form of Eq (1), where n = -0.31. No value of n is proposed here due to the sparsity and uncertainty of the data, and the previously proposed n = -0.31 appears to fit adequately. It is notable that the dissolution rates of both the synthetic fayalite and the fayalite slag show the same pH dependence, and absolute dissolution rates differ by less than one order of magnitude. The slightly higher fayalite slag dissolution rates may be due to presence of small quantities of amorphous iron silicate. In this context, the dissolution rates of the synthetic fayalite can be used to estimate the dissolution rates of the fayalite slag. In the case of LFS, the constituent phases generally consist of more than just γ -C₂S – the dissolution rates of the other constituent phases would need to be studied in order to estimate LFS dissolution rates.



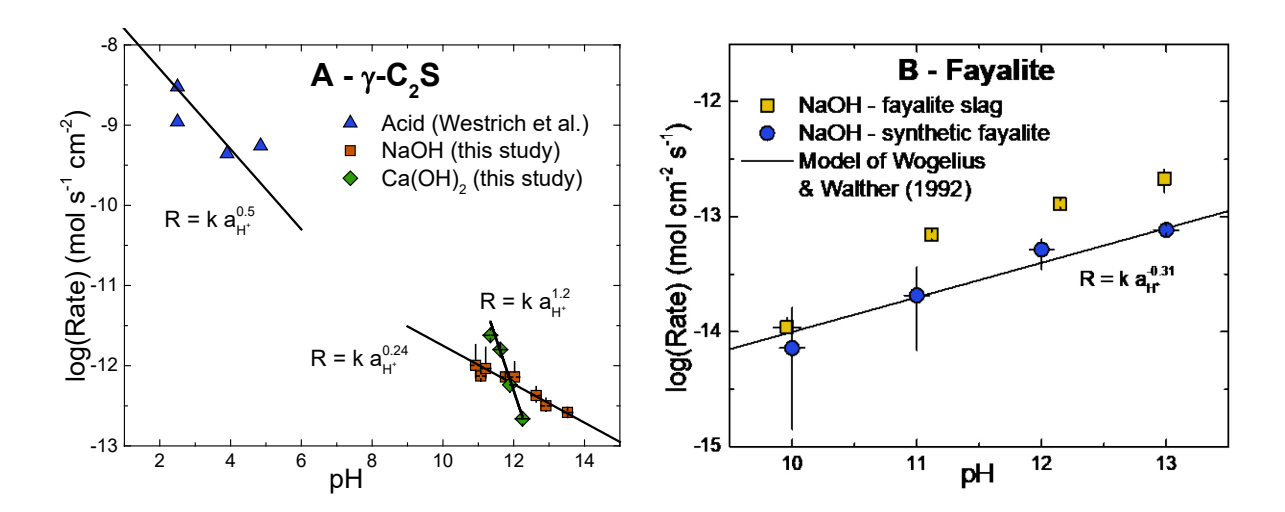


Figure 4. A: Rates of dissolution of γ - C_2S in NaOH, $Ca(OH)_2$ and acid solutions as a function of pH. B: Rates of dissolution of fayalite slag and synthetic fayalite in NaOH solution as a function of pH. Data in A is from [58], model in B is from [37]. The error bars represent minimum and maximum rates of triplicate experiments, where the major source of error is in measured Si concentrations across experiments.

The different dissolution rates of the olivines have in the past been explained in terms of the rate of hydration shell formation [25,58]. More rapid exchange of water from solvent into the hydration sphere of the dissolved cation correlate with higher dissolution rates. While the rate coefficient for water exchange from the solvent into the hydration sphere of Ca^{2+} is higher than that of Fe^{2+} [58], the different forms of pH dependence at pH > 10 means that γ -C₂S dissolution rates are slower than fayalite dissolution rates for pH > 10.

368

380

381

382

383

385

386

362

363

364

365

366

367

- The stronger pH dependence of dissolution rates in Ca(OH)₂ solution is due to the common-ion effect.
- 370 High concentrations of Ca already in solution slow dissolution of γ-C₂S by lowering the
- thermodynamic driving force for dissolution. Dissolution proceeds via the chemical reaction shown in
- 372 Eq (3);

373
$$Ca_2SiO_4(s) + 3H_2O(aq) \rightarrow 2Ca^{2+}(aq) + H_3SiO_4^-(aq) + 3OH^-(aq)$$
 (3)

- Eq (3) is irreversible under far from equilibrium conditions such as those described in this study. An
- often used general rate law for mineral dissolution is shown in Eq (4) [52];

$$Rate = -k_{+} \prod_{j} a_{X}^{m_{j}} \left[1 - e^{\frac{m\Delta G_{T}}{RT}} \right] = -k_{+} \prod_{j} a_{X}^{m_{j}} \left[1 - \left(\frac{IAP}{K_{CR}} \right)^{m} \right]$$

$$\tag{4}$$

where k_+ (mol cm⁻² s⁻¹) is the rate coefficient of the dissolution reaction, $a_X^{m_j}$ is the activity of aqueous species X in the rate-determining step (in this case, $\prod_j a_X^{m_j} = a_{H^+}^n$), m is a constant, ΔG_r is the Gibbs

free energy of reaction, R is the gas constant, T is the temperature, IAP is the ion activity product, and

 K_{SP} is the solubility product of the dissolution reaction. Smaller ion activity products correspond to a

system further from equilibrium with a stronger driving force for dissolution. In highly dilute systems,

such as the ones presented here, the ion activity product is assumed to remain constant during

dissolution as the dissolved aqueous species do not significantly change the ion activity product of the

384 solution over the course of the experiment. However, the ion activity product for Eq (3)

 $(a_{Ca^{2+}}^2 a_{H_3SiO_4^-} a_{OH^-}^3)$, is greater in Ca(OH)₂ solutions due to the large background concentration of

Ca ions already in solution. This is illustrated in Figure 5, where the ion activity product of each

solution (calculated in GEM-Selektor) is plotted as a function of pH. NaOH solutions have lower ion activity products therefore higher rates of dissolution than $Ca(OH)_2$ solutions of the same pH. These results are in contrast with Oelkers et al. who reported rates of forsterite (Mg₂SiO₄) to be independent of Mg and Si concentration [61]. However, their study was performed in acidic media and at lower cation and Si concentrations (<1.5 mM) than in this study. It is worth noting that Nicoleau et al. measured the change in dissolution rate as a function of ion activity product as a means of a calculating the solubility product, K_{SP} , for C_3S , β - C_2S , and CaO [62]. Calculating K_{SP} in this way requires more extensive measurements over a broader range of ion activity products than those presented in this study.

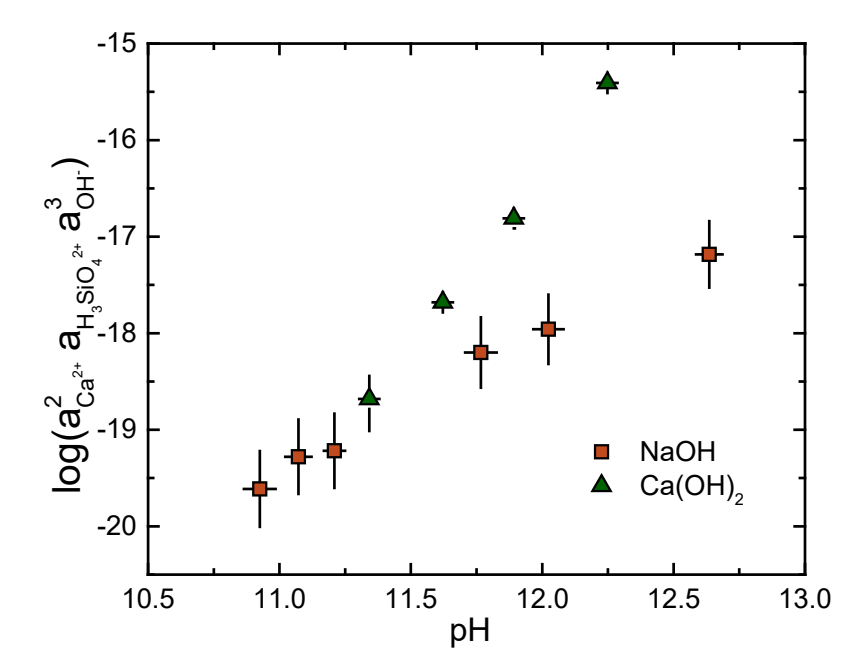


Figure 5. Ion activity products (based on Eq (3)) as a function of pH for NaOH and Ca $(OH)_2$ solutions. The error bars represent the minimum and maximum values of triplicate experiments.

405

406

407

408

409

410

411

412

413

414

415

416

417

418

419

420

421

422

423

424

425

426

427

428

429

403

Surface chemistry, as probed by XPS, provides insight into what limits dissolution of γ-C₂S and fayalite [60]. As described above, γ -C₂S powders were Ca deficient at the surface following exposure to NaOH solution. The Ca deficiency was more pronounced at lower pH and at later dissolution times. There are two possibilities for this Ca deficiency. The first possibility is Ca leaching from the surface, leaving a Si-rich skeleton at the surface. XPS studies of forsterite have shown a surface enriched in Mg in basic solutions, and surfaces deficient in Mg in acidic solutions [57,63–66]. These studies concluded that below pH 9, the surface is depleted in Mg due to an ion exchange reaction involving H⁺ ions from the solution, while in more alkaline solution, selective leaching of Si from olivine surfaces occurs. In the present study, Si-rich surfaces are observed in basic solution, meaning selective surface leaching is not the mechanism being observed here. A related phenomenon involves formation of an Si-rich layer at the surface of olivines and other calcium silicate minerals following exposure to solution. This phenomenon, first reported by Hellman et al. [67], is described as a coupled dissolution-precipitation reaction in which silica phases precipitate on the surface of the dissolving mineral. These porous layers do not necessarily hinder dissolution and can form in solutions in which anhydrous amorphous silica is undersaturated in the bulk solution, as is the case for the aqueous systems in this study [68,69]. Transition electron microscopy and energy dispersive X-ray analysis has identified a Si-rich surface layer of thickness <5 nm on weathered forsterite [70]. Si-rich layers have also been reported on the surface of other calcium silicate minerals, including wollastonite, β-C₂S, anorthite, and diopside [68,70,71]. This phenomenon most likely accounts for the observed Ca/Si ratios in the present study. The decrease in the Ca/Si ratio with time suggests continued growth of an amorphous silica layer on the surface of the particles over the timescale of the experiment. Additionally, at lower pH, there is more Si in solution available for the formation of such a layer resulting in a thicker layer than for particles exposed to higher pH solution. The leached layer and coupled interfacial dissolution-precipitation mechanisms need not be mutually exclusive – Maher et al. developed a framework that described mineral dissolution proceeding through formation of a

leached layer and newly precipitated amorphous layer on top of the leached layer [72]. A coupled dissolution-precipitation process has also been used to describe the dissolution of calcium-aluminosilicate glasses, which emphasized the undersaturation of reaction products with respect to bulk solution concentrations [73]. Further analysis of the surfaces through transmission electron microscopy is required to clarify this point.

XPS of the fayalite slag surface is shown in Figure 6. The oxidation state of iron pre-dissolution is shown as a function of depth into the surface in Figure 6A and the effect of exposure to NaOH is shown in Figure 6B. In both cases, argon milling into the surface successively removes surface material allowing the oxidation state of Fe beneath the surface to be revealed. In Figure 6A, deeper milling reveals a transition from Fe(III), characteristic of an oxidized surface layer, to Fe(II), characteristic of bulk fayalite. The intensities of the Fe2p_{1/2} and Fe2p_{3/2} shift from Fe(III) binding energies (710.8 eV in hematite) to lower binding energies associated with Fe(II) bonding (709.5 eV in wüstite) [74]. Similar shifts are seen in the satellite peaks of Fe2p_{1/2} and Fe2p_{3/2} as a function of depth. Figure 6B shows the XPS spectra of fayalite slag pre-dissolution, and fayalite slag after 7 days of NaOH exposure as a function of depth into the material. Post exposure to NaOH, Fe2p_{1/2} and Fe2p_{3/2} peaks shift to the left, indicating more Fe(III) bonding. This is understood to be due to the precipitation of goethite (Fe(III)O(OH)), which precipitates at very low Fe concentrations in basic solution. Argon milling of the NaOH exposed surface results in a shift back towards Fe(II) bonding, characteristic of bulk fayalite.

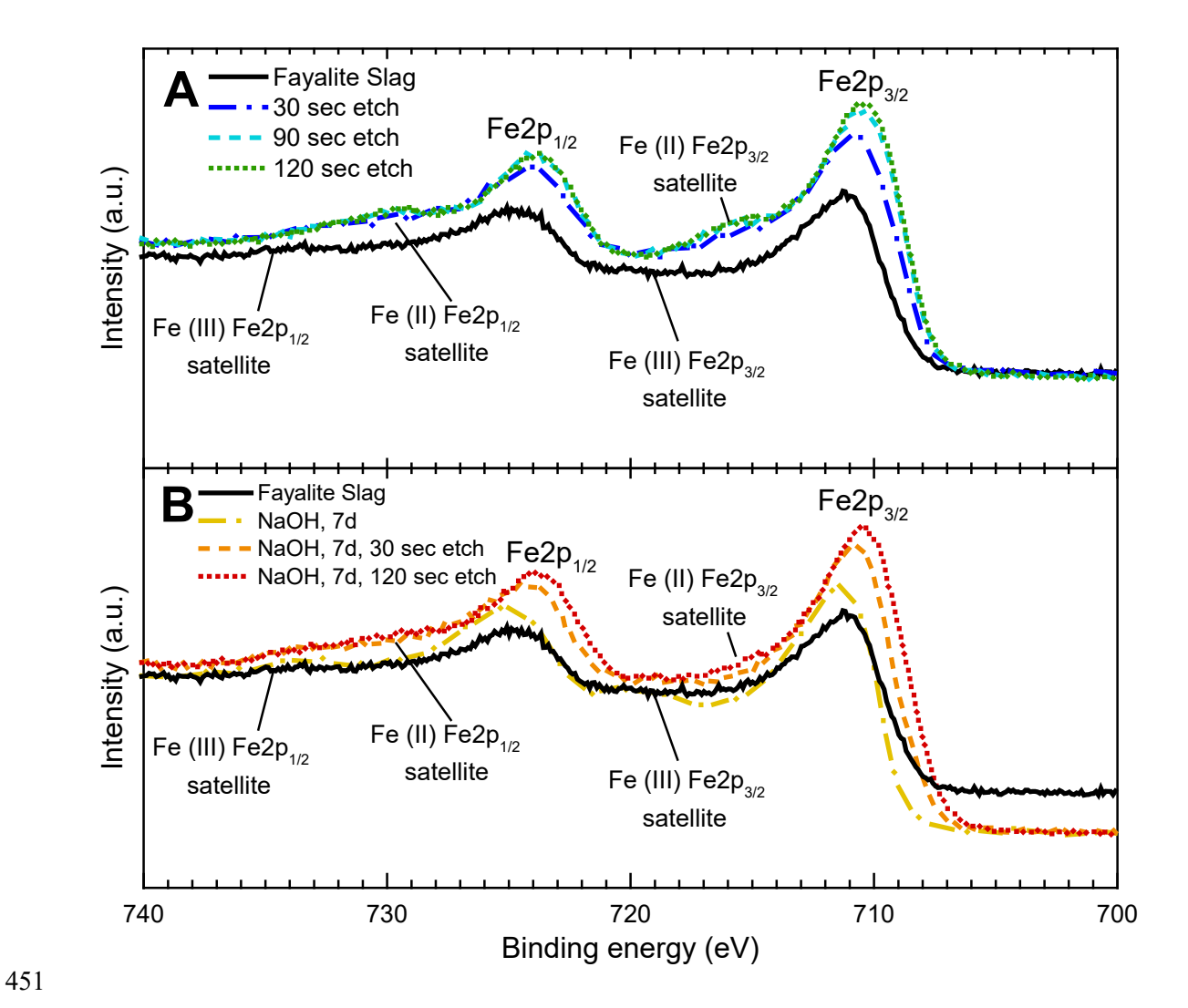


Figure 6. X-ray photoelectron spectra of $Fe2p_{1/2}$ and $Fe2p_{3/2}$ binding energies of fayalite slag surface. A: Argon milling into fayalite slag. B: Argon milling into fayalite slag following exposure to NaOH for 7 days.

The presence of an Fe(III) oxidized surface, in combination with a rapidly precipitating Fe hydroxide surface layer in basic solutions, results in a surface that has little resemblance to that of bulk fayalite. This difference manifests itself in a different dissolution rate dependence on pH than that of γ -C₂S. The formation of iron-containing precipitates on the surface of iron-bearing olivines has been identified previously. Comparing rates of dissolution of Mg₂SiO₄ with Mg_{1.8}Fe_{0.2}SiO₄, Golubev found the dissolution rate of the iron containing mineral to be an order of magnitude slower which was

attributed to precipitation of Fe(III) containing phases at the surface of the dissolving mineral [75]. Schott and Berner described cation depletion at the surface of fayalite in oxic and anoxic acidic solution [76,77]. In anoxic conditions, XPS revealed the surface to be deficient in iron after 30 days of exposure to pH 6 solution due to ion exchange of H⁺ ions for Fe²⁺ ions in the crystal structure. Under oxic conditions, the surface appeared to be enriched in iron.

467

462

463

464

465

466

5. Conclusions

469

470

471

472

473

474

475

476

477

478

479

480

481

482

483

484

485

486

487

468

Quantifying the rates of dissolution of ladle furnace steel slag and copper slag as a function of their aqueous environment offers insight into their expected reactivity in conventional or alternative concrete. Here, we quantify the reactivity of these slags through kinetic studies of their major phases from the olivine mineral group $-\gamma$ -C₂S and fayalite. γ -C₂S dissolution rates decreased with increasing pH, while fayalite dissolution rates increased with increasing pH. The reasons for the differing behavior was attributed to differences in the surface layers of the two minerals. γ-C₂S developed a Sirich surface layer which did not inhibit the overall dissolution. In contrast, an oxidized Fe(III) surface pre-dissolution combined with an iron hydroxide precipitate formed during dissolution to alter the form of the dependence of dissolution rate on pH. These results have strategic implications for the re-use of steel slags with high γ -C₂S contents and favalitic copper slags in concrete systems. One typical strategy to increase the dissolution rate of precursors in such systems is raising the pH of the aqueous phase of the binder, a process normally achieved through alkali activation. However, alkali activation of steel slags where γ-C₂S is the major phase will not improve the reactivity of the overall slag. Similarly, alkali activation of fayalitic copper slags will improve the reactivity of the slag but iron hydroxide will precipitate more quickly at higher pH, and gains in reactivity are unlikely to be sufficient to justify the use of an alkali activator. Improving our understanding of the reactivity of the major crystalline phases of alternative SCMs provides insight into strategies to derive benefit from their use.

488	
489	6. Acknowledgments
490	
491	We would like to acknowledge financial support for this research through the Environmental
492	Solutions Initiative, Massachusetts Institute of Technology, Cambridge. We also acknowledge support
493	from NSF CAREER #1751925. This work made use of the MRSEC Shared Experimental Facilities at
494	MIT, supported by the National Science Foundation under award number DMR-1419807, and
495	facilities at the Institute for Soldier Nanotechnologies (ISN) at MIT. This work was performed in part
496	at the Harvard University Center for Nanoscale Systems (CNS), a member of the National
497	Nanotechnology Coordinated Infrastructure Network (NNCI), which is supported by the National
498	Science Foundation under NSF award no. 1541959. Nicolas Chanut thanks Total S.A. for support.
499	The authors gratefully acknowledge Hindalco Industries for supplying the copper slag used in this
500	study. We thank Thomas Close for assistance in particle size distribution experiments featured in the
501	Supplementary Information.
502	
503	Conflict of interest
504	
505	The authors declare no conflicts of interest.
506	
507	References
508	
509	[1] S.J. Davis, N.S. Lewis, M. Shaner, S. Aggarwal, D. Arent, I.L. Azevedo, S.M. Benson, T.
510	Bradley, J. Brouwer, Y.M. Chiang, C.T.M. Clack, A. Cohen, S. Doig, J. Edmonds, P. Fennell,

C.B. Field, B. Hannegan, B.M. Hodge, M.I. Hoffert, E. Ingersoll, P. Jaramillo, K.S. Lackner,

- 512 K.J. Mach, M. Mastrandrea, J. Ogden, P.F. Peterson, D.L. Sanchez, D. Sperling, J. Stagner, J.E.
- Trancik, C.J. Yang, K. Caldeira, Net-zero emissions energy systems, Science (80-.). 360 (2018).
- 514 doi:10.1126/science.aas9793.
- 515 [2] K.L. Scrivener, V.M. John, E.M. Gartner, Eco-efficient cements: Potential economically viable
- solutions for a low-CO2 cement-based materials industry, Cem. Concr. Res. 114 (2018) 2–26.
- 517 doi:10.1016/j.cemconres.2018.03.015.
- 518 [3] R. Snellings, Assessing, understanding and unlocking supplementary cementitious materials,
- 519 RILEM Tech. Lett. 1 (2016) 50. doi:10.21809/rilemtechlett.2016.12.
- 520 [4] M.J. McCarthy, T. Robl, L.J. Csetenyi, Recovery, processing, and usage of wet-stored fly ash,
- in: Coal Combust. Prod. Charact. Util. Benef., Elsevier Ltd., 2017: pp. 343-367.
- 522 doi:10.1016/B978-0-08-100945-1.00014-9.
- 523 [5] M.C.G. Juenger, R. Snellings, S.A. Bernal, Supplementary cementitious materials: New sources,
- 524 characterization, and performance insights, Cem. Concr. Res. 122 (2019) 257–273.
- 525 doi:10.1016/j.cemconres.2019.05.008.
- 526 [6] H.G. van Oss, Iron and Steel Slag Mineral Commodity Summaries U.S. Geological Survey,
- 527 2019.
- 528 [7] International Copper Study Group, The World Copper Factbook 2018, 2018.
- 529 https://www.icsg.org/index.php/component/jdownloads/finish/170/2876.
- 530 [8] B. Gorai, R.K. Jana, Premchand, Characteristics and utilisation of copper slag A review,
- 531 Resour. Conserv. Recycl. 39 (2003) 299–313. doi:10.1016/S0921-3449(02)00171-4.
- 532 [9] M. Najimi, J. Sobhani, A.R. Pourkhorshidi, Durability of copper slag contained concrete
- exposed to sulfate attack, Constr. Build. Mater. 25 (2011) 1895–1905.
- 534 doi:10.1016/j.conbuildmat.2010.11.067.
- 535 [10] J. Setién, D. Hernández, J.J. González, Characterization of ladle furnace basic slag for use as a
- construction material, Constr. Build. Mater. 23 (2009) 1788–1794.

- 537 doi:10.1016/j.conbuildmat.2008.10.003.
- 538 [11] C. Shi, Characteristics and cementitious properties of ladle slag fines from steel production,
- 539 Cem. Concr. Res. 32 (2002) 459–462. doi:10.1016/S0008-8846(01)00707-4.
- 540 [12] D. Adolfsson, R. Robinson, F. Engström, B. Björkman, Influence of mineralogy on the hydraulic
- properties of ladle slag, Cem. Concr. Res. 41 (2011) 865-871.
- 542 doi:10.1016/j.cemconres.2011.04.003.
- 543 [13] W.C. Wang, H.Y. Wang, H.C. Tsai, Study on engineering properties of alkali-activated ladle
- furnace slag geopolymer, Constr. Build. Mater. 123 (2016) 800-805.
- 545 doi:10.1016/j.conbuildmat.2016.07.068.
- 546 [14] M. Salman, Ö. Cizer, Y. Pontikes, L. Vandewalle, B. Blanpain, K. Van Balen, Effect of curing
- 547 temperatures on the alkali activation of crystalline continuous casting stainless steel slag, Adv.
- 548 Cem. Res. 71 (2014) 308–316. doi:10.1016/j.conbuildmat.2014.08.067.
- 549 [15] C. Shi, C. Meyer, A. Behnood, Utilization of copper slag in cement and concrete, Resour.
- 550 Conserv. Recycl. 52 (2008) 1115–1120. doi:10.1016/j.resconrec.2008.06.008.
- 551 [16] K. Murari, R. Siddique, K.K. Jain, Use of waste copper slag, a sustainable material, J. Mater.
- 552 Cycles Waste Manag. 17 (2014) 13–26. doi:10.1007/s10163-014-0254-x.
- 553 [17] K.S. Al-Jabri, M. Hisada, S.K. Al-Oraimi, A.H. Al-Saidy, Copper slag as sand replacement for
- high performance concrete, Cem. Concr. Compos. 31 (2009) 483–488.
- doi:10.1016/j.cemconcomp.2009.04.007.
- 556 [18] K.S. Al-Jabri, R.A. Taha, A. Al-Hashmi, A.S. Al-Harthy, Effect of copper slag and cement by-
- pass dust addition on mechanical properties of concrete, Constr. Build. Mater. 20 (2006) 322–
- 558 331. doi:10.1016/j.conbuildmat.2005.01.020.
- 559 [19] A.M. Bhoi, Y.D. Patil, H.S. Patil, M.P. Kadam, Feasibility assessment of incorporating copper
- slag as a sand substitute to attain sustainable production perspective in concrete, Adv. Mater.
- 561 Sci. Eng. 2018 (2018) 1–11. doi:10.1155/2018/6502890.

- 562 [20] J.L. Provis, S.A. Bernal, RILEM State of the Art Report, 2014. doi:10.1007/978-94-007-7672-
- 563 2 5.
- 564 [21] A. Kuterasińska, J.; Król, Mechanical properties of alkali-acivated binders based on copper slag,
- 565 Archit. Civ. Eng. Environ. 3 (2015) 61–67.
- 566 [22] S. Onisei, A.P. Douvalis, A. Malfliet, A. Peys, Y. Pontikes, Inorganic polymers made of fayalite
- slag: On the microstructure and behavior of Fe, J. Am. Ceram. Soc. 101 (2018) 2245–2257.
- 568 doi:10.1111/jace.15420.
- 569 [23] A. Nazer, J. Payá, M.V. Borrachero, J. Monzó, Use of ancient copper slags in Portland cement
- and alkali activated cement matrices, J. Environ. Manage. 167 (2016) 115-123.
- 571 doi:10.1016/j.jenvman.2015.11.024.
- 572 [24] H. Uvegi, P. Chaunsali, B. Traynor, E. Olivetti, Reactivity of industrial wastes as measured
- 573 through ICP-OES: A case study on siliceous Indian biomass ash, J. Am. Ceram. Soc. (2019) 1–
- 574 11. doi:10.1111/jace.16628.
- 575 [25] J. Skibsted, R. Snellings, Reactivity of supplementary cementitious materials (SCMs) in cement
- 576 blends, Cem. Concr. Res. 124 (2019) 105799. doi:10.1016/j.cemconres.2019.105799.
- 577 [26] A. Lazaro, H.J.H. Brouwers, G. Quercia, J.W. Geus, The properties of amorphous nano-silica
- 578 synthesized by the dissolution of olivine, Chem. Eng. J. 211–212 (2012) 112–121.
- 579 doi:10.1016/j.cej.2012.09.042.
- 580 [27] A. Lazaro, L. Benac-Vegas, H.J.H. Brouwers, J.W. Geus, J. Bastida, The kinetics of the olivine
- dissolution under the extreme conditions of nano-silica production, Appl. Geochemistry. 52
- 582 (2015) 1–15. doi:10.1016/j.apgeochem.2014.10.015.
- 583 [28] X. Gao, Q.L. Yu, A. Lazaro, H.J.H. Brouwers, Investigation on a green olivine nano-silica
- source based activator in alkali activated slag-fly ash blends: Reaction kinetics, gel structure and
- 585 carbon footprint, Cem. Concr. Res. 100 (2017) 129–139. doi:10.1016/j.cemconres.2017.06.007.
- 586 [29] E.H. Oelkers, J. Declercq, G.D. Saldi, S.R. Gislason, J. Schott, Olivine dissolution rates: A

- 587 critical review, Chem. Geol. 500 (2018) 1–19. doi:10.1016/j.chemgeo.2018.10.008.
- 588 [30] F.K. Crundwell, The mechanism of dissolution of forsterite, olivine and minerals of the
- orthosilicate group, Hydrometallurgy. 150 (2014) 68–82. doi:10.1016/j.hydromet.2014.09.006.
- 590 [31] J.D. Rimstidt, S.L. Brantley, A.A. Olsen, Systematic review of forsterite dissolution rate data,
- 591 Geochim. Cosmochim. Acta. 99 (2012) 159–178. doi:10.1016/j.gca.2012.09.019.
- 592 [32] R.A. Wogelius, J. V. Walther, Olivine dissolution at 25°C: Effects of pH, CO2, and organic
- 593 acids, Geochim. Cosmochim. Acta. 55 (1991) 943–954. doi:10.1016/0016-7037(91)90153-V.
- 594 [33] E.H. Oelkers, General kinetic description of multioxide silicate mineral and glass dissolution,
- 595 Geochim. Cosmochim. Acta. 65 (2001) 3703–3719. doi:10.1016/S0016-7037(01)00710-4.
- 596 [34] J. Bensted, Gamma-dicalcium silicate and its hydraulicity, Cem. Concr. Res. 8 (1978) 73–76.
- 597 [35] R. Trettin, G. Oliew, C. Stadelmann, W. Wieker, Very early age hydration of dicalcium silicate-
- 598 polymorphs, Cem. Concr. Res. 21 (1991) 757–764.
- 599 [36] L. Kriskova, Y. Pontikes, F. Zhang, Ö. Cizer, P.T. Jones, K. Van Balen, B. Blanpain, Influence
- of mechanical and chemical activation on the hydraulic properties of gamma dicalcium silicate,
- 601 Cem. Concr. Res. 55 (2014) 59–68. doi:10.1016/j.cemconres.2013.10.004.
- 602 [37] R.A. Wogelius, J. V. Walther, Olivine dissolution kinetics at near-surface conditions, Chem.
- 603 Geol. 97 (1992) 101–112. doi:10.1016/0009-2541(92)90138-U.
- 604 [38] D. Daval, D. Testemale, N. Recham, J.M. Tarascon, J. Siebert, I. Martinez, F. Guyot, Fayalite
- (Fe2SiO4) dissolution kinetics determined by X-ray absorption spectroscopy, Chem. Geol. 275
- 606 (2010) 161–175. doi:10.1016/j.chemgeo.2010.05.005.
- 607 [39] L. Duro, F. El Aamrani, M. Rovira, J. Giménez, I. Casas, J. De Pablo, J. Bruno, The dissolution
- of high-FeO oliving rock from the Lovasjärvi intrusion (SE-Finland) at 25°C as a function of
- pH, Appl. Geochemistry. 20 (2005) 1284–1291. doi:10.1016/j.apgeochem.2005.03.004.
- 610 [40] T.L.O. Sunde, T. Grande, M.A. Einarsrud, Modified Pechini synthesis of oxide powders and

- thin films, in: Handb. Sol-Gel Sci. Technol., 2016: pp. 1–30. doi:10.1007/978-3-319-19454-7.
- 612 [41] I. Nettleship, J.L. Shull, W.M. Kriven, Chemical preparation and phase stability of Ca2SiO4 and
- 613 Sr2SiO4 powders, J. Eur. Ceram. Soc. 11 (1993) 291–298.
- 614 [42] H.M. Rietveld, A profile refinement method for nuclear and magnetic structures, J. Appl.
- 615 Crystallogr. 2 (1969) 65–71. doi:10.1107/s0021889869006558.
- 616 [43] S. Brunauer, P.H. Emmett, E. Teller, Adsorption of gases in multimolecular layers, J. Am.
- 617 Chem. Soc. 60 (1938) 309–319. doi:10.1021/ja01269a023.
- 618 [44] W.C. Records, Y. Yoon, J.F. Ohmura, N. Chanut, A.M. Belcher, Virus-templated Pt–Ni(OH) 2
- nanonetworks for enhanced electrocatalytic reduction of water, Nano Energy. 58 (2019) 167–
- 620 174. doi:10.1016/j.nanoen.2018.12.083.
- 621 [45] D.A. Kulik, T. Wagner, S. V Dmytrieva, G. Kosakowski, F.F. Hingerl, K. V Chudnenko, U.R.
- Berner, GEM-Selektor geochemical modeling package: revised algorithm and GEMS3K
- numerical kernel for coupled simulation codes, Comput. Geosci. 17 (2013) 1–24.
- 624 doi:10.1007/s10596-012-9310-6.
- 625 [46] T. Wagner, D.A. Kulik, F.F. Hingerl, S. V Dmytrieva, GEM-Selektor geochemical modeling
- package: TSolMod library and data interface for multicomponent phase models, Can. Mineral.
- 50 (2012) 1173–1195. http://dx.doi.org/10.3749/canmin.50.5.1173.
- 628 [47] T. Thoenen, W. Hummel, U.R. Berner, E. Curti, The PSI/Nagra Chemical Thermodynamic
- Database 12/07, Villigen PSI, Switzerland, 2014.
- 630 [48] B. Lothenbach, D.A. Kulik, T. Matschei, M. Balonis, L. Baquerizo, B.Z. Dilnesa, G.D. Miron,
- M. R., Cemdata18: A chemical thermodynamic database for hydrated Portland cements and
- alkali-activated materials., Cem. Concr. Res. 115 (2018) 472–506.
- 633 doi:10.1109/ICCPS.2014.6843714.
- 634 [49] H.C. Helgeson, D.H. Kirkham, G.C. Flowers, Theoretical prediction of the thermodynamic
- behavior of-aqueous electrolytes at high pressures and temperatures: IV. Calculation of activity

- coefficients, osmotic coefficients, and apparent molal and standard and relative partial molal
- 637 properties to 600C, Am. J. Sci. 281 (1981) 1249–1516.
- 638 [50] R.J. Myers, S.A. Bernal, J.L. Provis, A thermodynamic model for C-(N-)A-S-H gel: CNASH-
- 639 ss. Derivation and validation, Cem. Concr. Res. 66 (2014) 27–47.
- doi:10.1016/j.cemconres.2014.07.005.
- 641 [51] A.C. Lasaga, A. Luttge, Variation of crystal dissolution rate based on a dissolution stepwave
- model, Science (80-.). 291 (2001) 2400–2405.
- 643 [52] K.L. Nagy, A.C. Lasaga, Dissolution and precipitation kinetics of gibbsite at 80°C and pH 3:
- The dependence on solution saturation state, Geochim. Cosmochim. Acta. 56 (1992) 3093–
- 645 3111. doi:10.1016/0016-7037(92)90291-P.
- 646 [53] A. Luttge, E. Bolton, A.C. Lasaga, An interferometric study of the dissolution kinetics of
- anorthite: The role of reactive surface area, Am. J. Sci. 299 (1999) 652-678.
- 648 doi:10.2475/ajs.299.7-9.652.
- 649 [54] O.S. Pokrovsky, J. Schott, Kinetics and mechanism of forsterite dissolution at 25 ° C and pH
- 650 from 1 to 12, Geochim. Cosmochim. Acta. 64 (2000) 3313–3325.
- 651 [55] R.A. Berner, J. Schott, Mechanism of pyroxene and amphibole weathering II observations of
- 652 soil grains, Am. J. Sci. 282 (1982) 1214–1231.
- 653 [56] M.F.J. Hochella, A.H. Carim, A reassessment of electron escape depths in silicon and thermally
- grown silicon dioxide thin films, Surf. Sci. 197 (1988) 260–268.
- 655 [57] V.P. Zakaznova-Herzog, H.W. Nesbitt, G.M. Bancroft, J.S. Tse, Characterization of leached
- layers on olivine and pyroxenes using high-resolution XPS and density functional calculations,
- 657 Geochim. Cosmochim. Acta. 72 (2008) 69–86. doi:10.1016/j.gca.2007.09.031.
- 658 [58] H.R. Westrich, R.T. Cygan, W.H. Casey, C. Zemitis, G.W. Arnold, The dissolution kinetics of
- 659 mixed-cation orthosilicate minerals, Am. J. Sci. 293 (1993) 869–893.
- doi:10.2475/ajs.293.9.869.

- 661 [59] P. V. Brady, J. V. Walther, Controls on silicate dissolution rates in neutral and basic pH solutions
- at 25°C, Geochim. Cosmochim. Acta. 53 (1989) 2823–2830. doi:10.1016/0016-7037(89)90160-
- 663 9.
- 664 [60] A. Blum, A.C. Lasaga, Role of surface speciation in the low-temperature dissolution of minerals,
- 665 Nature. 331 (1988) 431–433.
- 666 [61] E.H. Oelkers, An experimental study of forsterite dissolution rates as a function of temperature
- and aqueous Mg and Si concentrations, Chem. Geol. 175 (2001) 485–494. doi:10.1016/S0009-
- 668 2541(00)00352-1.
- 669 [62] L. Nicoleau, A. Nonat, D. Perrey, The di- and tricalcium silicate dissolutions, Cem. Concr. Res.
- 47 (2013) 14–30. doi:10.1016/j.cemconres.2013.01.017.
- 671 [63] O.S. Pokrovsky, J. Schott, Forsterite surface composition in aqueous solutions: A combined
- potentiometric, electrokinetic, and spectroscopic approach, Geochim. Cosmochim. Acta. 64
- 673 (2000) 3299–3312. doi:10.1016/S0016-7037(00)00435-X.
- 674 [64] K. Fujimoto, K. Fukutani, M. Tsunoda, H. Yamashita, K. Kobayashi, Hydrogen depth profiling
- using the 1H(15 N, αγ) 12 C reaction in stainless steel pre-irradiated with helium ions, Geochem.
- 676 J. 27 (1993) 155–162. doi:10.13182/fst88-a25219.
- 677 [65] H. Seyama, M. Soma, A. Tanaka, Surface characterization of acid-leached olivines by X-ray
- photoelectron spectroscopy, Chem. Geol. 129 (1996) 209-216. doi:10.1016/0009-
- 679 2541(95)00142-5.
- 680 [66] R.W. Luce, R.W. Bartlett, G.A. Parks, Dissolution kinetics of magnesium silicates, Geochim.
- 681 Cosmochim. Acta. 36 (1972) 35–50. doi:10.1016/0016-7037(72)90119-6.
- 682 [67] R. Hellmann, J.M. Penisson, R.L. Hervig, J.H. Thomassin, M.F. Abrioux, An EFTEM/HRTEM
- high-resolution study of the near surface of labradorite feldspar altered at acid pH: Evidence for
- interfacial dissolution-reprecipitation, Phys. Chem. Miner. 30 (2003) 192–197.
- doi:10.1007/s00269-003-0308-4.

- 686 [68] E. Ruiz-Agudo, C. V. Putnis, C. Rodriguez-Navarro, A. Putnis, Mechanism of leached layer
- formation during chemical weathering of silicate minerals, Geology. 40 (2012) 947–950.
- 688 doi:10.1130/G33339.1.
- 689 [69] E. Ruiz-Agudo, C. V. Putnis, A. Putnis, Coupled dissolution and precipitation at mineral-fluid
- 690 interfaces, Chem. Geol. 383 (2014) 132–146. doi:10.1016/j.chemgeo.2014.06.007.
- 691 [70] R. Hellmann, R. Wirth, D. Daval, J.P. Barnes, J.M. Penisson, D. Tisserand, T. Epicier, B. Florin,
- R.L. Hervig, Unifying natural and laboratory chemical weathering with interfacial dissolution-
- reprecipitation: A study based on the nanometer-scale chemistry of fluid-silicate interfaces,
- 694 Chem. Geol. 294–295 (2012) 203–216. doi:10.1016/j.chemgeo.2011.12.002.
- 695 [71] A.S. Brand, J.M. Gorham, J.W. Bullard, Dissolution rate spectra of β-dicalcium silicate in water
- of varying activity, Cem. Concr. Res. 118 (2019) 69–83. doi:10.1016/j.cemconres.2019.02.014.
- 697 [72] K. Maher, N.C. Johnson, A. Jackson, L.N. Lammers, A.B. Torchinsky, K.L. Weaver, D.K. Bird,
- 698 G.E. Brown, A spatially resolved surface kinetic model for forsterite dissolution, Geochim.
- 699 Cosmochim. Acta. 174 (2016) 313–334. doi:10.1016/j.gca.2015.11.019.
- 700 [73] K.C. Newlands, M. Foss, T. Matschei, J. Skibsted, D.E. Macphee, Early stage dissolution
- characteristics of aluminosilicate glasses with blast furnace slag- and fly-ash-like compositions,
- 702 J. Am. Ceram. Soc. 100 (2017) 1941–1955. doi:10.1111/jace.14716.
- 703 [74] A.P. Grosvenor, B.A. Kobe, M.C. Biesinger, N.S. Mcintyre, Investigation of multiplet splitting
- of Fe 2p XPS spectra and bonding in iron compounds, Surf. Interface Anal. 36 (2004) 1564–
- 705 1574. doi:10.1002/sia.1984.
- 706 [75] S. V. Golubev, O.S. Pokrovsky, J. Schott, Experimental determination of the effect of dissolved
- 707 CO2 on the dissolution kinetics of Mg and Ca silicates at 25 °C, Chem. Geol. 217 (2005) 227–
- 708 238. doi:10.1016/j.chemgeo.2004.12.011.
- 709 [76] J. Schott, R.A. Berner, X-ray photoelectron studies of the mechanism of iron silicate dissolution
- 710 during weathering, Geochim. Cosmochim. Acta. 47 (1983) 2233–2240. doi:10.1016/0016-

711 7037(83)90046-7.

712 [77] J. Schott, R.A. Berner, Dissolution mechanisms of pyroxenes and olivines during weathering,

713 in: Chem. Weather., 1985: pp. 35–53.